Research Article

Cancer Immunology Research

PD-L1 microSPECT/CT Imaging for Longitudinal Monitoring of PD-L1 Expression in Syngeneic and Humanized Mouse Models for Cancer

Sandra Heskamp[1], Peter J. Wierstra[1], Janneke D.M. Molkenboer-Kuenen[1], Gerwin W. Sandker[1], Soley Thordardottir[2], Jeannette Cany[2], Daniel Olive[3], Johan Bussink[4], Otto C. Boerman[1], Harry Dolstra[2], Erik H.J.G. Aarntzen[1], and Willemijn A. Hobo[2]

Abstract

Antibodies that block the interaction between programmed death ligand 1 (PD-L1) and PD-1 have shown impressive responses in subgroups of patients with cancer. PD-L1 expression in tumors seems to be a prerequisite for treatment response. However, PD-L1 is heterogeneously expressed within tumor lesions and may change upon disease progression and treatment. Imaging of PD-L1 could aid in patient selection. Previously, we showed the feasibility to image PD-L1$^+$ tumors in immunodeficient mice. However, PD-L1 is also expressed on immune cell subsets. Therefore, the aim of this study was to assess the potential of PD-L1 micro single-photon emission tomography/computed tomography (microSPECT/CT) using radiolabeled PD-L1 antibodies to (i) measure PD-L1 expression in two immunocompetent tumor models (syngeneic mice and humanized mice harboring PD-L1 expressing immune cells) and (ii) monitor therapy-induced changes in tumor PD-L1 expression. We showed that radiolabeled PD-L1 antibodies accumulated preferentially in PD-L1$^+$ tumors, despite considerable uptake in certain normal lymphoid tissues (spleen and lymph nodes) and nonlymphoid tissues (duodenum and brown fat). PD-L1 microSPECT/CT imaging could also distinguish between high and low PD-L1–expressing tumors. The presence of PD-L1$^+$ immune cells did not compromise tumor uptake of the human PD-L1 antibodies in humanized mice, and we demonstrated that radiotherapy-induced upregulation of PD-L1 expression in murine tumors could be monitored with microSPECT/CT imaging. Together, these data demonstrate that PD-L1 microSPECT/CT is a sensitive technique to detect variations in tumor PD-L1 expression, and in the future, this technique may enable patient selection for PD-1/PD-L1–targeted therapy.

Introduction

In the past years, checkpoint blockade has shown impressive efficacy in the treatment of patients with cancer. In this anticancer therapy, boosting of tumor-attacking T cells plays a critical role. Effective activation of tumor-reactive T cells requires (i) T-cell receptor recognition of the corresponding epitope presented by the major histocompatibility complex and (ii) signaling via costimulatory molecules, such as CD28, following interaction with their cognate ligands (i.e., CD80/86) expressed by the antigen-presenting cells. The magnitude and duration of the T-cell response is further regulated by coinhibitory signaling molecules, including programmed death-1 (PD-1; ref. 1). PD-1 is expressed by activated T cells and has two ligands, programmed death ligand-1 (PD-L1) and PD-L2. Upon triggering, PD-1 transduces an inhibitory signal into the T cell, resulting in reduced T-cell proliferation, decreased secretion of effector cytokines, and potentially exhaustion. By upregulating PD-L1, tumors can escape immune recognition and attack (2–4).

PD-L1 is expressed on a wide variety of tumors (5). Clinical trials with immune-checkpoint inhibitors (ICI), including anti–PD-1 and anti–PD-L1, have shown impressive and durable (>1 year) responses in patients with advanced tumors, including non–small cell lung cancer (NSCLC), melanoma, Hodgkin and non-Hodgkin lymphoma, head and neck (H&N) cancer, and renal cell cancer (6–15). Despite these encouraging developments, not all patients respond to ICI. As a result, nonresponding patients are unnecessarily exposed to ineffective and expensive treatment, while alternative treatment is delayed. Immune-related adverse events also occur frequently and require immune-suppressive treatment in serious cases, e.g., in pneumonitis, colitis, and pancreatitis (16–18).

Hence, an urgent need for a biomarker to accurately predict ICI therapy response is needed. Several studies have demonstrated that patients with PD-L1$^+$ tumors are more likely to respond to ICI (6, 13, 19–22). Currently, PD-L1 expression in tumors is generally determined by IHC. However, this method

[1]Department of Radiology and Nuclear Medicine, Radboud Institute of Molecular Life Sciences, Radboud University Medical Center, Nijmegen, the Netherlands. [2]Laboratory Medicine, Laboratory of Hematology, Radboud University Medical Center, Nijmegen, the Netherlands. [3]CRCM, Immunity and Cancer, Inserm, U1068, Institut Paoli-Calmettes, Aix-Marseille Université, UM 105, CNRS, UMR7258, Marseille, France. [4]Department of Radiation Oncology, Radboud University Medical Center, Nijmegen, the Netherlands.

Note: Supplementary data for this article are available at Cancer Immunology Research Online (http://cancerimmunolres.aacrjournals.org/).

Corresponding Author: Sandra Heskamp, Radboud University Medical Center, P.O. Box 9101, 6500 HB Nijmegen, the Netherlands. Phone: 31-24-36-14511; E-mail: Sandra.Heskamp@radboudumc.nl

doi: 10.1158/2326-6066.CIR-18-0280

has limitations. First, there are no standard procedures (e.g., antibody clone, staining protocol) and strict criteria to define PD-L1 positivity (23). Second, analysis on archival tissue must be interpreted with caution because PD-L1 expression is a dynamic phenomenon that could change over time due to alterations in the tumor microenvironment and/or treatment (24–33). Finally, PD-L1 expression is very heterogeneous within and between tumor lesions (19, 34–39). In contrast, molecular imaging allows analysis of whole tumor lesions and metastases, thereby avoiding sampling errors and misinterpretation due to intratumoral and interlesional heterogeneity. It enables quantitative and longitudinal monitoring of PD-L1 expression without the need of repeated invasive biopsies. Therefore, it could potentially serve as a predictive biomarker to select patients for ICI therapy or as a tool to monitor PD-L1 expression during conventional anticancer treatments.

Previously, we have shown the feasibility of imaging PD-L1 expressing human xenograft tumors in immunodeficient mice using radiolabeled PD-L1 antibodies and micro single-photon emission tomography/computed tomography (micro-SPECT/CT; ref. 40). However, in patients, PD-L1 is also expressed on subsets of immune cells and other healthy tissues. Targeting of these cells could result in a high background signal and may limit visualization of PD-L1$^+$ tumors. In this study, we demonstrated the feasibility of imaging PD-L1 in different immunocompetent tumor models: (i) syngeneic mice and (ii) humanized mice harboring PD-L1 expressing immune cells. We also demonstrated the potential of this noninvasive imaging technique to monitor therapy-induced changes in PD-L1 expression by the tumor cells.

Materials and Methods

Cell culture

MDA-MB-231 (human breast carcinoma, ATCC), Renca (murine renal cell carcinoma, ATCC), CT26 (murine colon carcinoma, kind gift from Dr. G. J. Peters of the Vrije Universiteit Amsterdam), and B16F1 (murine melanoma, kind gift from Dr. M. Schreurs of the Department of Tumor Immunology, Radboudumc) cell lines were cultured in RPMI 1640 (GIBCO, BRL Life Sciences Technologies), supplemented with 2 mmol/L glutamine (GIBCO) and 10% fetal calf serum (FCS, Sigma-Aldrich Chemie BV) at 37°C in a humidified atmosphere with 5% CO_2. 4T1 cells (murine breast carcinoma, ATCC) were cultured in RPMI 1640, 2 mmol/L glutamine, 10 mmol/L HEPES (GIBCO), and 1 mmol/L pyruvate (GIBCO). LLC1 cells (murine lung carcinoma, ATCC) were cultured in DMEM, glucose (4500 mg/L; GIBCO), 2 mmol/L glutamine, and 10% FCS. All cell lines were tested negative for mycoplasma. The number of passages between thawing and use in experiment was ≤ 10. The MDA-MB-231 cell line was authenticated using STR profiling by Eurofins Genomics according to ANSI/ATCC standard ASN-0002 (08-11-2016).

Radiolabeling

The following antibodies were conjugated with isothiocyanatobenzyl-diethylenetriaminepentaacetic acid (ITC-DTPA, Macrocyclics) and subsequently radiolabeled with indium-111 (^{111}In, Curium), as described previously (40): murine IgG1 anti-human PD-L1 (anti–hPD-L1, clone PD-L1.3.1; ref. 41), rat IgG2b anti-murine PD-L1 (anti–mPD-L1, clone 10F.9G2, Bio X Cell), murine IgG1 irrelevant control antibody (mIgG1, clone MOPC-21, Bio X Cell), and rat IgG2a irrelevant control antibody (rIgG2, clone 2A3, Bio X Cell). Radiochemical purity exceeded 91% for all *in vitro* experiments and 94% for all animal experiments.

In vitro assays

MDA-MB-231, Renca, 4T1, B16F1, LLC1, and CT26 cells were cultured to confluency in 6-well plates and incubated with 700 Bequerel (Bq) ^{111}In–anti–hPD-L1 (26 pmol/L), ^{111}In-mIgG1 (185 pmol/L), ^{111}In–anti–mPD-L1 (14-39 pmol/L), or ^{111}In-rIgG2 (39 pmol/L) for 4 hours at 37°C in RPMI1640 containing 0.5% BSA. Nonspecific binding of the radiolabeled antibodies was determined by coincubation with 6.7 nmol/L unlabeled anti–hPD-L1, mIgG1, anti–mPD-L1, or rIgG2. After incubation, cells were washed with PBS, and the cell-associated activity was measured in a shielded well-type gamma counter (Perkin-Elmer).

The immunoreactive fraction (IRF), 50% inhibitory concentration (IC_{50}), dissociation constant (K_d), PD-L1 receptor density, and internalization kinetics of ^{111}In–anti–mPD-L1 were determined as described previously (40). In short, IRF was determined using a serial dilution of 4.6×10^4 to 1.2×10^7 Renca cells in RPMI 1640 containing 0.5% BSA, upon incubation with 140 Bq ^{111}In–anti–mPD-L1 (12 pmol/L). For the IC_{50} determination, Renca cells were incubated for 4 hours on ice with 700 Bq ^{111}In–anti–mPD-L1 (6.7 pmol/L) and increasing concentrations of unlabeled anti–mPD-L1 (10–3,000 pmol/L). To determine the K_d and receptor density, Scatchard analysis was performed with Renca, 4T1, B16F1, CT26, and LLC1 cells upon a 4-hour incubation on ice with increasing concentrations of ^{111}In–anti–mPD-L1 (3–1,000 pmol/L) in 1 mL RPMI 1640 containing 0.5% BSA. Internalization kinetics were studied using Renca cells that were incubated for 2, 4, or 24 hours with 700 kBq ^{111}In–anti–mPD-L1 (40 pmol/L) at 37°C in a humidified atmosphere with 5% CO_2. The IRF of ^{111}In–anti–hPD-L1 was 82%, IC_{50} was 0.15 nmol/L, K_d was 0.97 nmol/L, and after 24 hours of incubation, 25% of the cell-associated activity was internalized, and 75% was still membrane-bound (40).

Animal experiments

Mice. All studies were conducted in accordance with the principles laid out by the Dutch Act on Animal Experiments (2014) and approved by the Animal Welfare Body of the Radboud University Nijmegen and Central Authority for Scientific Procedures on Animals. Mice were housed in individually ventilated cages with a filter top (Blue line IVC, Tecniplast) under pathogen-free conditions with cage enrichment present, and were fed and watered *ad libitum*. Experiments with murine tumor models were performed using female BALB/c or C57BL/6 mice (6–8 weeks, Janvier). Studies with humanized mice were performed using female NOD/SCID-IL2Rγnull (NSG) mice (6–12 weeks), originally purchased from The Jackson Laboratories, which were housed and bred in the Radboudumc Central Animal Laboratory. Tumor-bearing mice were block-randomized into groups based on tumor size.

Dose optimization and pharmacokinetics of ^{111}In–anti–mPD-L1. BALB/c mice were inoculated subcutaneously with Renca tumors (5×10^5 cells in 0.2 mL RPMI). When tumors reached a size of approximately 0.2 cm^3, mice received an intravenous injection

of 0.2 MBq ^{111}In–anti–mPD-L1 in the tail vein. To study the effect of the antibody protein dose on the biodistribution and tumor uptake of ^{111}In–anti–mPD-L1, groups received escalating antibody doses of anti–mPD-L1 (1–1,000 μg/mouse) or 30 μg ^{111}In-labeled rat isotype–matched control IgG (0.2 MBq). At 1, 3, or 7 days after injection, mice were euthanized using CO_2/O_2 asphyxiation. The biodistribution of the radiolabel in tumor and normal tissue was determined *ex vivo*, as described previously (40).

PD-L1 microSPECT/CT imaging in healthy mice and syngeneic murine tumor models. BALB/c mice were inoculated with Renca (5×10^5 cells), 4T1 (1×10^6 cells), or CT26 (1×10^6 cells), and C57BL/6 mice were inoculated with B16F1 (2.5×10^6 cells) or LLC1 (5×10^5 cells). Tumor-bearing and non–tumor-bearing mice ($n = 5$ per group) received 30 μg ^{111}In–anti–mPD-L1 (19.7 ± 1.2 MBq). Three days later, mice were euthanized by CO_2/O_2 asphyxiation and SPECT/CT images were acquired with the U-SPECT-II/CT system (MILabs; ref. 42). Mice were scanned for 30 to 40 minutes using the 1.0-mm diameter pinhole mouse high-sensitivity collimator tube, followed by a CT scan (spatial resolution 160 μm, 65 kV, 615 μA) for anatomical reference. Scans were reconstructed (MILabs reconstruction software v2.04), using an ordered-subset expectation maximization algorithm, with a voxel size of 0.2 mm. SPECT/CT scans were analyzed and maximum intensity projections (MIP) were created using the Inveon Research Workplace software v4.1. A 3D volume of interest was drawn around the tumor and organs of interest. Uptake was quantified as the percentage injected dose per gram (%ID/g), assuming a tissue density of 1 g/cm^3. After the SPECT scan, mice were dissected to quantify the uptake in tumor and normal tissue, as described previously (40).

PD-L1 microSPECT/CT imaging in tumor-bearing humanized mice. CD34$^+$ hematopoietic stem cells (HSC) were obtained from human umbilical cord blood collected after normal full-term delivery and written informed consent (CMO 2014/226) using CD34 MACS Microbeads (Miltenyi Biotech), following the manufacturer's instructions.

NSG mice were irradiated with a sublethal dose of 2.5 Gy to eradicate murine HSCs in bone marrow to facilitate effective engraftment. The next day, mice were anesthetized and transplanted intrafemurally with 50,000 CD34$^+$ human HSCs (5 μL). Prior to transplantation, mice were injected subcutaneously with buprenorphine (0.05 mg/kg) as an analgesic. Seven weeks after transplantation, blood samples were collected via tail puncture to determine the human immune cell engraftment for group allocation. At week 8, mice were inoculated subcutaneously with 5×10^6 MDA-MB-231 cells (mixed 2:1 with matrigel, BD Biosciences, Pharmingen). At week 11, mice were injected intraperitoneally with lipopolysacharide (LPS; 0.6 mg/kg) to induce PD-L1 upregulation on myeloid/monocytic cells. One day after LPS administration, mice were injected intravenously with 11.9 ± 1.6 MBq (1 μg) ^{111}In–anti–hPD-L1 or 11.5 ± 0.4 MBq (2.8 μg) ^{111}In-labeled control mIgG1. Three days later, mice were euthanized by CO_2/O_2 asphyxiation. SPECT/CT images were acquired for 30 to 45 minutes and analyzed as described above.

An additional group of mice was included to assess the PD-L1 expression by different subsets of human immune cells *ex vivo*. The same experimental procedure was followed as described above, except for the injection of the radiolabeled antibody. One day before LPS injection, and 1 and 4 days after LPS injection, mice were euthanized and blood, spleen, and bone marrow were collected to evaluate human immune cell engraftment and to assess the expression of PD-L1 on different myeloid/monocytic cell subsets by flow cytometry ($n = 3$ per group).

PD-L1 microSPECT/CT imaging to monitor radiotherapy-induced changes in PD-L1 expression. BALB/c mice were inoculated subcutaneously with CT26 cells ($n = 12$) and C57BL/6 mice were inoculated with B16/F1 ($n = 12$) or LLC1 cells ($n = 12$) in the right hind legs. Half of the mice were anesthetized, and tumors were irradiated with a single dose of 10 Gy (320 kV; dose rate, 3.8 Gy/minute; X-RAD; RPS Services Limited; ref. 43). The next day, mice were injected with 23.8 ± 1.7 MBq ^{111}In–anti–mPD-L1 (30 μg). The following day, mice were euthanized followed by microSPECT/CT imaging and *ex vivo* biodistribution as described above. Tumor tissue was stored in 4% formalin to determine PD-L1 expression immunohistochemically.

Flow cytometry

Leukocytes were enriched from blood, spleen, and bone marrow using ammonium chloride solution or by lympholyte-MM density centrifugation (Cedarlane). Next, cells were washed and incubated for 10 minutes on ice in PBS containing total human IgG (1 mg/L; Sanquin Blood Bank) and brilliant violet staining buffer (BD Horizon). Subsequently, cells were labeled with the following antibodies: hCD45-KO or -BUV395 (Beckman Coulter clone J.33 and BD Biosciences clone HI30, respectively), mCD45-AF700 or -BV605 (both BD Biosciences clone 30-F11), CD11c-PECy7 (BioLegend clone 3.9), CD14-APC or -BV711 (BioLegend clone RMO52 or BD Biosciences clone MφP9, respectively) and BDCA1-BV421 or -APC-Cy7 (both BioLegend clone L161) in combination with PD-L1-PE (BD Biosciences clone MIH1) or mIgG1-PE isotype control (BioLegend clone MOPC-21) for 30 minutes on ice. Subsequently, cells were washed and stained for 10 minutes with eFluor780 (eBioscience) or Sytox blue (Invitrogen) viability dye. Finally, cells were analyzed on a Gallios flow cytometer (Beckman Coulter) or FACSAria (BD Biosciences). Data were analyzed using Kaluza software v1.5a. Single cells were gated based on forward/side scatter characteristics. Subsequently, PD-L1 expression was analyzed on the following viable myeloid/monocytic cell populations: BDCA1$^+$ myeloid DCs (BDCA1$^+$CD11c$^+$ mDC), monocytes (CD14$^+$CD11c$^+$), and (immature) myeloid cells (CD45^{dim}SS^{hi}).

IHC

PD-L1 expression in tumors and normal tissues was determined on paraffin-embedded tissue sections. In short, antigen retrieval was performed in 10 mmol/L sodium citrate, sections were preincubated with 10% normal rabbit serum, and endogenous peroxidase activity was blocked with 3% H_2O_2. Subsequently, anti–mPD-L1 (0.4 μg/mL, AF1019; R&D Systems) was applied and tissues were incubated overnight at 4°C. Next, sections were incubated with biotinylated anti-goat IgG (3.75 μg/mL E0466, DAKO) followed by incubation with avidin–biotin–enzyme complexes (dilution 1:50, Vector Laboratories). Finally, 3′,3′-diaminobenzidine (DAB) was used to develop the tumor sections. Tumor sections were scored into three categories: PD-L1–negative (no membrane staining), low PD-L1 expression

(weak membrane staining), and high PD-L1 expression (strong membrane staining).

Statistical analyses

Statistical analyses were performed using PASW Statistics version 18.0 and GraphPad Prism version 5.03 for Windows. Data are presented as mean ± standard deviation, unless stated otherwise. Differences in uptake of the radiolabeled antibodies were tested for significance using a one-way ANOVA. A *P* value below 0.05 was considered significant.

Results

^{111}In–anti–mPD-L1 and ^{111}In–anti–hPD-L1 specifically bind to PD-L1^{+} tumor cells *in vitro*

To evaluate the binding specificity of the radiolabeled antibodies, *in vitro* binding studies were performed using various cancer cell lines. We observed efficient binding of ^{111}In–anti–mPD-L1 and ^{111}In–anti–hPD-L1 to PD-L1^{+} Renca and MDA-MB-231 tumor cells, respectively (Fig. 1A). This was blocked by treatment with excess unlabeled anti–mPD-L1 or anti–hPD-L1, demonstrating the binding specificity of the radiolabeled antibodies for PD-L1, and radiolabeled isotype control antibodies did not bind to these PD-L1^{+} tumors cells. ^{111}In–anti–mPD-L1 showed the highest binding to Renca cells, followed by B16F1, 4T1, LLC1, and CT26 (Fig. 1B). This binding capacity paralleled the expression of PD-L1 on the tumor cells: Renca: 60,500 ± 1,800 receptors/cell, B16F1: 7,200 ± 140 receptors/cell, 4T1: 4,000 ± 280 receptors/cell, LLC1: 780 ± 40 receptors/cell, and CT26: 62 ± 5 receptors/cell. Based on these results, Renca cells were used for further *in vitro* experiments to characterize the ^{111}In-labeled antibody. The IRF (fraction of the radiolabeled antibody which is capable of binding PD-L1) of ^{111}In–anti–mPD-L1 was 91%, and anti–mPD-L1 showed high affinity for mPD-L1 with an IC_{50} of 1.33 nmol/L (unlabeled anti–mPD-L1, Fig. 1C) and K_d of 1.1 ± 0.1 nmol/L (^{111}In-anti–mPD-L1). Finally, we observed that after a 24-hour incubation, 41% ± 0.4% of the cell-associated activity was internalized, whereas the remaining 59% ± 0.4% was still membrane bound (Fig. 1D). Together, these data demonstrated that ^{111}In–anti–mPD-L1 specifically binds to PD-L1–expressing tumor cells.

^{111}In–anti–mPD-L1 specifically accumulates in PD-L1^{+} tissues *in vivo*

To evaluate *in vivo* targeting of PD-L1^{+} tumors, we first performed a dose-escalation study to determine the optimal antibody dose. We demonstrated that ^{111}In–anti–mPD-L1 specifically accumulated in PD-L1^{+} Renca tumors. Tumor uptake of 30 μg ^{111}In–anti–mPD-L1 was significantly higher compared with 30 μg of irrelevant IgG ($P < 0.001$; Fig. 2A). PD-L1–specific uptake was observed in several other organs, including lymphoid tissues (spleen and lymph nodes) and nonlymphoid tissues (brown fat and duodenum). The highest tumor uptake was observed in mice injected with 30 μg of ^{111}In–anti–mPD-L1 (22.4 ± 2.1 %ID/g). At antibody dosages <30 μg,

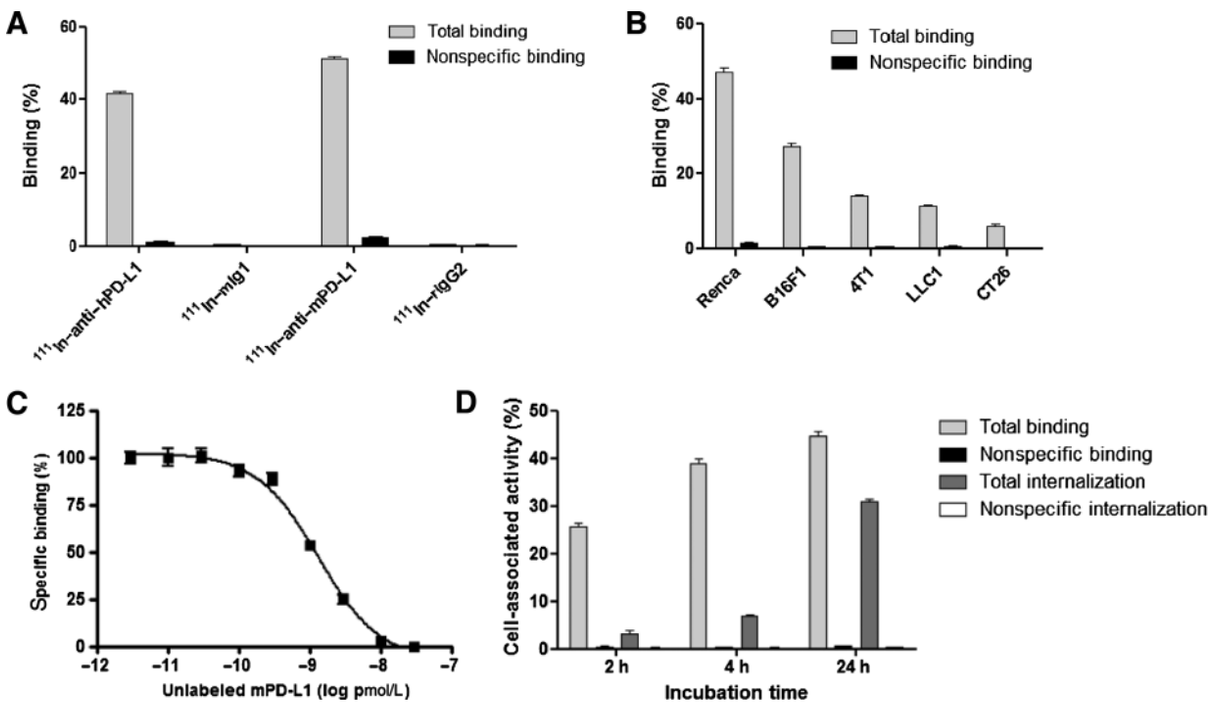

Figure 1.

^{111}In–anti–mPD-L1 and ^{111}In–anti–hPD-L1 specifically bind to PD-L1^{+} tumor cells *in vitro*. **A,** Total and nonspecific binding of ^{111}In–anti–hPD-L1 and ^{111}In–anti–mIgG1 to MDA-MB-231 cells and ^{111}In-anti–mPD-L1 and ^{111}In-rIgG2 to Renca cells. **B,** Binding of ^{111}In–anti–mPD-L1 to five different murine cancer cell lines. **C,** IC_{50} analysis of ^{111}In–anti–mPD-L1 on Renca cells. **D,** Internalization analysis of ^{111}In–anti–mPD-L1 on Renca cells. *, Nonspecific binding and internalization was determined by coincubation with an excess of the unlabeled antibody.

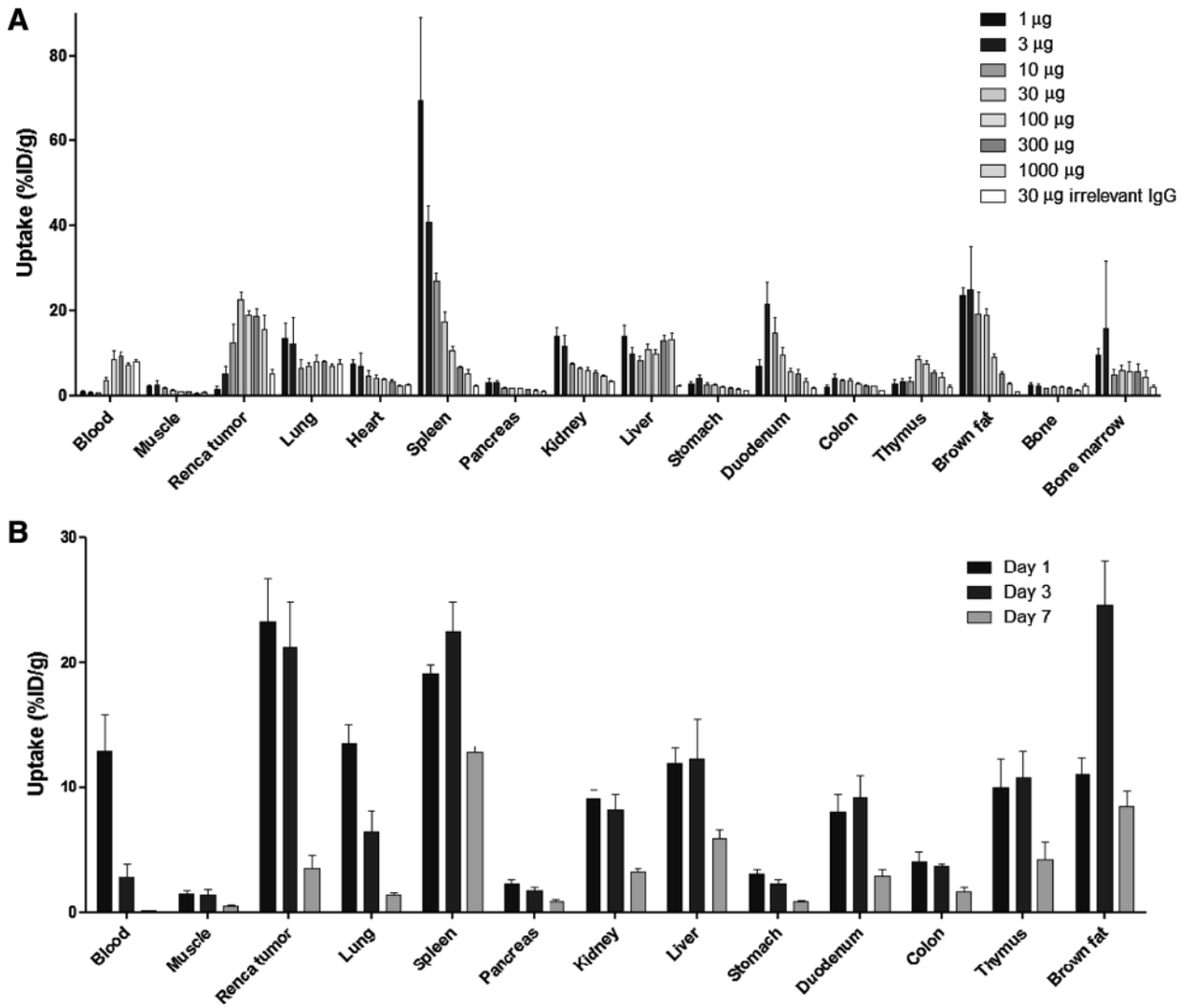

Figure 2.

^{111}In–anti–mPD-L1 specifically accumulates in PD-L1^{+} tissues *in vivo*. **A,** Dose-escalation study in BALB/c mice with subcutaneous Renca tumors at 3 days after injection of 0.2 MBq ^{111}In–anti–mPD-L1 ($n = 6$ mice/group). **B,** Biodistribution analysis of ^{111}In–anti–mPD-L1 (30 µg) in BALB/c mice with subcutaneous Renca tumors at 1, 3, and 7 days after injection ($n = 5$ mice/group).

^{111}In–anti–mPD-L1 was rapidly cleared from the circulation, resulting in low tumor uptake. In contrast, spleen uptake was highest at 1 µg (69.4 ± 19.6 %ID/g) but decreased with increasing dosages (30 µg: 17.4 ± 2.3 %ID/g). Although the irrelevant control IgG showed similar concentrations in blood as the ^{111}In–anti–mPD-L1, uptake in tumor (5.1 ± 1.1 %ID/g), as well as other organs such as spleen, duodenum, and brown fat, was significantly lower (all $P < 0.001$). Based on these results, 30 µg ^{111}In–anti–mPD-L1 was used in further studies. Here, we demonstrated that tumor uptake was highest at 1 and 3 days after injection (23.3 ± 3.5 %ID/g and 21.3 ± 3.7 %ID/g, respectively) and decreased to 3.5 ± 1.1 %ID/g at day 7 (Fig. 2B). Again, we observed rapid clearance of ^{111}In–anti–mPD-L1 from the circulation with concentrations in blood of 12.8 ± 3.0 %ID/g, 2.8 ± 1.1 %ID/g, and 0.12 ± 0.02 %ID/g at days 1, 3, and 7 after injection, respectively. Together, these data demonstrated the effective and specific accumulation of ^{111}In–anti–mPD-L1 in tumor and several normal tissues such as spleen, duodenum, and brown fat.

^{111}In–anti–mPD-L1 microSPECT/CT discriminates high from low PD-L1–expressing tumors

To assess the sensitivity of ^{111}In–anti–mPD-L1 imaging, uptake in different tumors with varying PD-L1 expression was studied using microSPECT/CT. The highest *in vivo* uptake of ^{111}In–anti–mPD-L1 was found in Renca, B16F1, and 4T1 tumors, whereas lower uptake was observed in CT26 and LLC1 tumors (Fig. 3A). In accordance, *ex vivo* biodistribution analysis confirmed the highest uptake in Renca (14.5 ± 5.5 %ID/g), B16F1 (14.9 ± 4.0 %ID/g), and 4T1 (16.3 ± 5.7 %ID/g), whereas uptake in CT26 and LLC1 tumors was 11.1 ± 6.5 and 6.2 ± 2.9 %ID/g, respectively (one-way ANOVA, $P = 0.033$). Full biodistribution data are described in Supplementary Table S1. Similarly, IHC demonstrated high PD-L1 expression

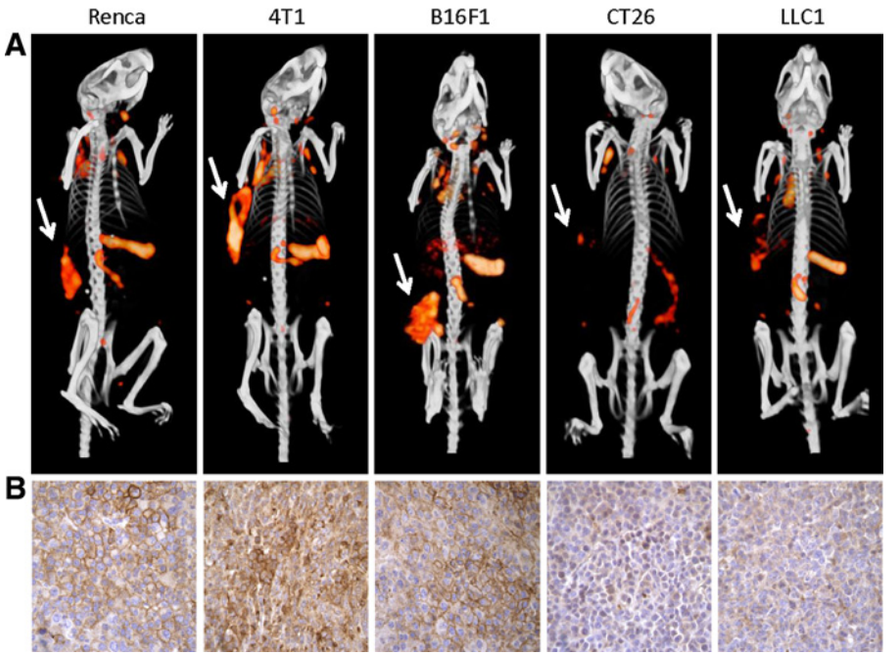

Figure 3.
^{111}In–anti–mPD-L1 microSPECT/CT discriminates high PD-L1–expressing tumors from low PD-L1–expressing tumors. **A,** MicroSPECT/CT images of mice with subcutaneous Renca, 4T1, B16F1, CT26, and LLC1 tumors injected with 30 μg ^{111}In–anti–mPD-L1 acquired 3 days after injection. Tumors are indicated by arrows. MicroSPECT/CT images are MIPs thresholded to illustrate which tissues show most pronounced uptake of ^{111}In–anti–mPD-L1 (the same thresholding was applied for all images, $n = 5$ mice/group) **B,** Corresponding IHC analysis of PD-L1 expression of the tumors.

on the tumor cell membrane for Renca, B16F1, and 4T1, and low-to-negative PD-L1 expression for CT26 and LLC1 tumors, which correlated with the microSPECT/CT findings (Fig. 3B). In addition to high tumor uptake, microSPECT/CT imaging also demonstrated uptake of ^{111}In–anti–mPD-L1 in spleen, duodenum, brown fat, and lymph nodes (Fig. 4A), and IHC confirmed PD-L1 expression in these healthy tissues (Fig. 4B). Finally, to evaluate the impact of tumor presence on the biodistribution of ^{111}In–anti–mPD-L1, we compared the uptake pattern in tumor-bearing versus non–tumor-bearing mice. We did not observe differences in normal tissue uptake between these groups in both BALB/c and C57BL/6 mice. Typical examples are shown in Fig. 4, and full biodistribution data are described in Supplementary Table S2. These data illustrate the sensitivity of PD-L1 microSPECT/CT to detect tumors with varying PD-L1 expression.

MicroSPECT/CT visualizes PD-L1$^+$ human xenografts and lymphoid tissues in humanized mice

To allow translation of our findings to the human setting, we next studied ^{111}In–anti–hPD-L1 microSPECT/CT imaging in humanized mice bearing MDA-MB-231 xenografts. We observed efficient engraftment of human immune cells after 12 weeks with 8.63% ± 7.8% (blood), 37.1% ± 23.5% (bone marrow), and 38.1% ± 25.1% (spleen) of leukocytes being of human origin (Supplementary Fig. S1). Nonhumanized mice revealed high uptake of ^{111}In–anti–anti–hPD-L1 in MDA-MB-231 xenografts, whereas accumulation was low in normal tissues. Similarly, we also observed high uptake of ^{111}In–anti–hPD-L1 in tumors of humanized mice. Although three out of five mice showed similar biodistribution in normal tissues as the nonhumanized mice, the two other mice showed increased uptake in spleen and lymph nodes. Activation of human immune cells by LPS further enhanced uptake of ^{111}In–anti–hPD-L1 in the spleen, lymph nodes, and bone marrow (Fig. 5A and B). Tumor uptake was not affected by LPS treatment as visualized by the high tumor to normal tissue contrast in all mice.

To demonstrate that the increased uptake in spleen was PD-L1 mediated, an additional study was performed using ^{111}In-labeled anti–hPD-L1 or an irrelevant isotype control antibody. MicroSPECT/CT imaging, again, demonstrated increased spleen uptake of ^{111}In–anti–hPD-L1 in LPS-treated humanized mice (27.1 ± 8.9 %ID/g) compared with non-humanized mice (9.7 ± 1.0 %ID/g, $P = 0.008$), whereas tumor uptake remained similar. Increased spleen targeting was not observed for ^{111}In-IgG in LPS-stimulated versus nonstimulated humanized mice ($P = 0.26$). Spleen uptake of ^{111}In–anti–mPD-L1 in LPS-treated humanized mice was significantly higher compared with spleen uptake in LPS-treated nonhumanized mice ($P = 0.043$). These results indicate that the enhanced splenic uptake can be specifically attributed to PD-L1 expression (Supplementary Fig. S2).

Spleen, blood, and bone marrow samples were collected prior to, and 1 and 4 days after LPS injection to analyze PD-L1 expression by flow cytometry. PD-L1 was upregulated on monocytes, myeloid dendritic cells, and immature myeloid cells in the spleen (Fig. 5C), explaining the increased uptake of ^{111}In–anti–hPD-L1 *in vivo* following LPS stimulation. Although less pronounced, upregulation of PD-L1 was also observed in bone marrow and peripheral blood (Supplementary Fig. S3). The LPS-mediated upregulation of PD-L1 on activated immune cells was greatest 1 day after treatment, at the time when radiolabeled antibody was normally administered. After 4 days, PD-L1 expression returned almost back to normal for monocytes and myeloid DCs, whereas myeloid cells still retained increased expression. Together, these data demonstrated that despite the presence of activated PD-L1–expressing human immune cells, visualization of PD-L1$^+$ tumors is feasible.

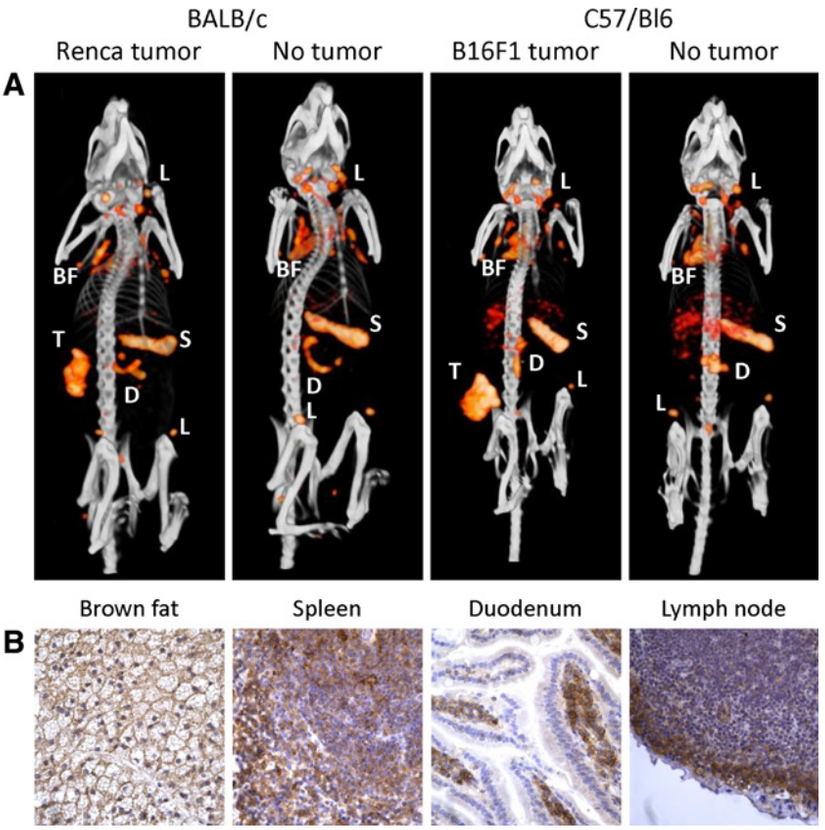

Figure 4.
Distribution of ^{111}In–anti–mPD-L1 in tumor-bearing versus non–tumor-bearing mice. **A,** MicroSPECT/CT images of BALB/c mice with or without a PD-L1^{+} Renca tumors, and C57BL/6 mice with or without a PD-L1^{+} B16F1 tumor 3 days after injection of 30 μg ^{111}In–anti–mPD-L1. MicroSPECT/CT images are MIPs thresholded to illustrate which tissues show most pronounced uptake of ^{111}In–anti–mPD-L1 (the same thresholding was applied for all images). Uptake of ^{111}In–anti–mPD-L1 was observed in tumors (T), spleen (S), duodenum (D), lymph nodes (L), and brown fat (BF). **B,** IHC analysis of PD-L1 expression in healthy tissues (brown fat, spleen, duodenum, and lymph node).

MicroSPECT/CT monitors radiotherapy-mediated upregulation of PD-L1 expression

Finally, we evaluated the regulation of PD-L1 expression on tumor cells in response to radiotherapy. To this end, CT26 tumor-bearing mice were subjected to irradiation and injected 1 day later with ^{111}In–anti–mPD-L1. We observed significantly increased uptake of ^{111}In–anti–mPD-L1 in irradiated CT26 tumors compared with nonirradiated tumors (26.3 ± 2.0 versus 17.1 ± 3.1 %IDg, $P = 0.003$, Fig. 6A). A similar effect, although less pronounced, was observed for LLC1 (15.7 ± 1.8 vs. 12.3 ± 1.7 %ID/g, $P = 0.033$). In contrast, B16F1 tumors did not show significantly altered tracer uptake upon irradiation (irradiated: 14.9 ± 6.8 %ID/g vs. nonirradiated: 16.7 ± 3.5). IHC staining confirmed that the increased tumor uptake in CT26 and LLC1 tumors was related to enhanced PD-L1 expression (Fig. 6B). Quantitative analysis of the microSPECT/CT scans also revealed enhanced uptake in the tumor-draining lymph node following radiotherapy in LLC1 and B16F1 tumor-bearing mice (LLC1: 11.6 ± 1.7 vs. 9.0 ± 0.8 %ID/g, $P = 0.036$; B16F1: 13.1 ± 1.7 vs. 7.6 ± 1.2 %ID/g, $P = 0.002$). Splenic uptake was not affected by tumor irradiation in any of the models (Fig. 6C). To conclude, these data demonstrated that therapy-related alteration of PD-L1 expression can be sensitively monitored using ^{111}In–anti–mPD-L1 microSPECT/CT.

Discussion

ICI therapy with anti–PD-1/PD-L1 antibodies has shown impressive efficacy with significantly improved overall survival in patients with cancer. However, not all patients respond to these therapies. Currently, there is no accurate biomarker to predict treatment response, although PD-L1^{+} tumors are more likely to respond than PD-L1^{-} tumors. Here, we demonstrated that PD-L1 microSPECT/CT is a sensitive technique to evaluate the presence and dynamics of PD-L1 expression in tumors and normal tissues, and to monitor treatment-induced changes in tumor PD-L1 expression.

Our *in vitro* studies demonstrated that ^{111}In–anti–mPD-L1 has excellent characteristics for *in vivo* imaging. First, the immunoreactivity is retained after radiolabeling, and the affinity for mPD-L1 is high. Upon binding of ^{111}In–anti–mPD-L1 to PD-L1 on the tumor cells, the antibody is internalized. Upon internalization and degradation of the antibody, ^{111}In-DTPA is trapped inside and, thus, accumulates over time. This will result in enhanced tumor-to-background contrast during SPECT/CT imaging (44). Similar observations were previously made for ^{111}In–anti–hPD-L1 (40).

Our *in vivo* studies showed that the optimal antibody dose of ^{111}In–anti–mPD-L1 to target PD-L1^{+} tumors was 30 μg. At lower dosages, the radiolabeled antibody was rapidly cleared from the circulation. By increasing the antibody dose, PD-L1–mediated uptake in spleen could be saturated, resulting in enhanced concentrations of circulating antibody in blood, and thereby allowing higher uptake of ^{111}In–anti–mPD-L1 in PD-L1^{+} tumors. In humans, it is well known that PD-L1 is also expressed on subsets of immune cells, mainly myeloid cells, including dendritic cells and monocytes. Because the presence of these cells may hamper the visualization of PD-L1^{+} tumors, we also determined

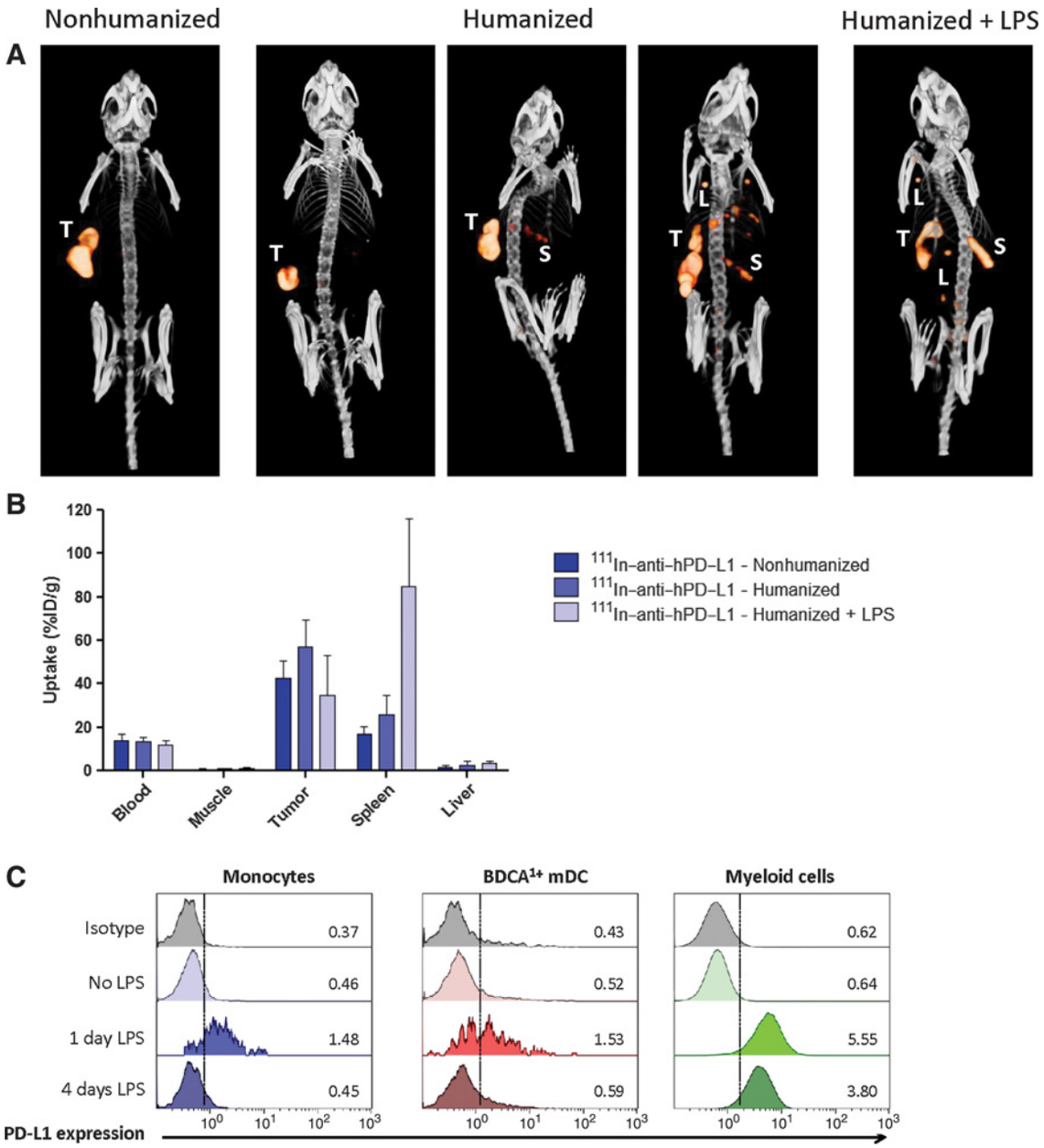

Figure 5.

^{111}In–anti–hPD-L1 microSPECT/CT visualizes PD-L1^{+} human xenografts and PD-L1^{+} lymphoid tissues in humanized mice. **A,** MicroSPECT/CT images (MIPs thresholded to illustrate which tissues show most pronounced uptake of ^{111}In–anti–hPD-L1, the same thresholding was applied for all images) and **B,** *ex vivo* biodistribution of mice bearing subcutaneous MDA-MB-213 xenografts at 3 days after ^{111}In–anti–hPD-L1 injection (i.e., 4 days after LPS treatment, $n = 5$–6 mice/group). Uptake was observed in tumors (T), spleen (S), and lymph nodes (L). **C,** PD-L1 expression on myeloid and monocytic immune cell subsets isolated from spleens at 1 and 4 days after LPS injection ($n = 3$ mice/group). Numbers in the plot represent the mean fluorescence intensity.

the effect of human PD-L1–expressing immune cells on the tumor uptake of ^{111}In–anti–hPD-L1. To this end, we established a humanized mouse model with xenograft tumors. Previously, we reported that the optimal dose of ^{111}In–anti–hPD-L1 to image PD-L1^{+} xenografts in immunodeficient mice was $\leq$ 1 μg/mouse. In humanized mice, we observed that despite high uptake of ^{111}In–anti–hPD-L1 in lymphoid tissues, the tumor uptake was not negatively affected by the presence of PD-L1–expressing immune cells. LPS treatment, to induce inflammation-mediated activation and maturation of the myeloid cells, resulted in upregulation of PD-L1 expression and corresponded with enhanced accumulation of ^{111}In–anti–hPD-L1 in spleen and lymph nodes, and this did not hamper the visualization of PD-L1^{+} xenografts. The radiolabeled irrelevant

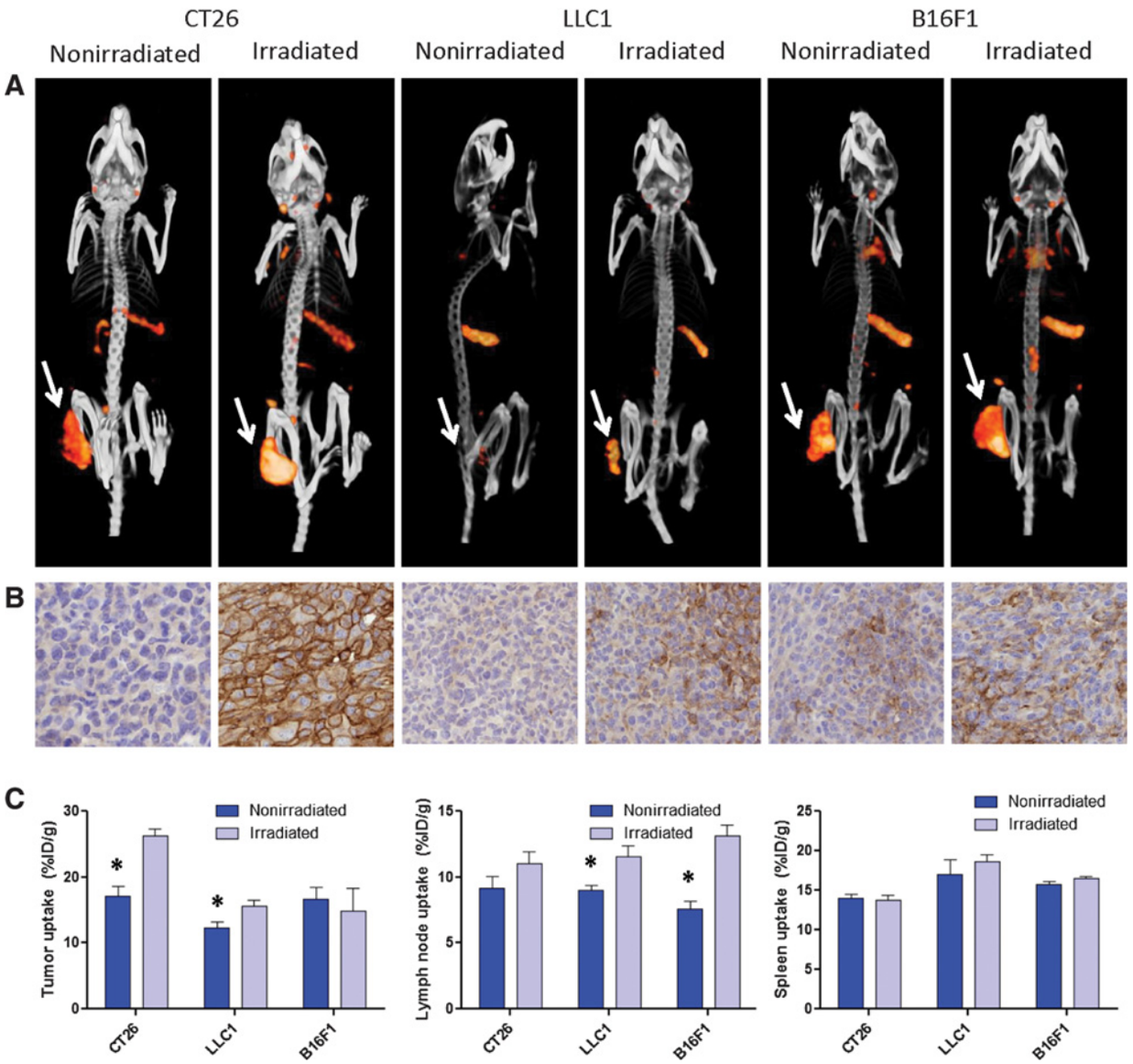

Figure 6.

^{111}In–anti–mPD-L1 microSPECT/CT is a sensitive technique to monitor radiotherapy-mediated upregulation of PD-L1 expression. **A,** MicroSPECT/CT images of mice with irradiated (10 Gy) or nonirradiated tumors 1 day after injection of 30 μg ^{111}In–anti–mPD-L1. Tumors are indicated by arrows. MicroSPECT/CT images are MIPs thresholded to illustrate which tissues show most pronounced uptake of ^{111}In–anti–mPD-L1 (the same thresholding was applied for all images). **B,** IHC analysis of PD-L1 expression by these tumors. **C,** Quantification of the uptake of ^{111}In–anti–mPD-L1 in tumors, lymph nodes, and spleen ($n = 4$ mice/group). *, Significant difference between the groups ($P < 0.05$).

control IgG did not show significant uptake in tumor, spleen, nor lymph node, supporting the specificity of ^{111}In–anti–m/hPD-L1.

In the past years, several groups have published radiotracers for noninvasive imaging of PD-L1–expressing tumors in mice. Radiotracers directed against human PD-L1 have been evaluated in immunodeficient mice bearing PD-L1–expressing human xenografts, using radiolabeled antibodies (MPDL3280A, atezolizumab, PD-L1.3.1), small, high-affinity engineered protein scaffolds (HACA-PD1), peptides (WL12), and Affibody molecules ($Z_{PD\text{-}L1\_1}$; refs. 40, 45–49). Although these studies demonstrate proof-of-principle that PD-L1 imaging is feasible, the translational relevance is hampered by the fact that in these models, uptake in PD-L1$^+$ tumors versus healthy tissues and the impact of (PD-L1 expressing) immune cells could not be evaluated. So far, three studies have reported the use of an mPD-L1 antibody to image PD-L1 expression in syngeneic murine tumor models (50–52). These studies also demonstrated the importance of selecting an appropriate antibody dose to saturate PD-L1 expression on healthy tissues to improve the circulation time and superior accumulation of the PD-L1 antibody in the tumor (51, 52). In accordance with our findings, Hettich and colleagues demonstrated PD-L1–specific

uptake in spleen, lymph nodes, and brown fat using a ^{64}Cu-labeled mPD-L1 antibody, although uptake in duodenum was not seen in these studies. Subsequently, flow-cytometric analysis showed that PD-L1 was primarily expressed by leukocytes (both macrophages and T cells) present in brown fat, and nearly absent on adipocytes. Broos and colleagues developed ^{99m}Tc-labeled nanobodies for microSPECT/CT imaging of PD-L1–expressing murine tumors and showed PD-L1–specific uptake in tumor, spleen, lymph nodes, brown fat, lungs, heart, and thymus. No selective uptake was reported in duodenum (53).

Here, we also demonstrated that a single dose of 10 Gy X-rays induced upregulation of PD-L1 expression in CT26 and LLC1 tumors, whereas no significant changes were observed in B16F1 tumors. Similarly, Kikuchi and colleagues showed that using ^{89}Zr-labeled anti–mPD-L1 increases tumor PD-L1 expression in a syngeneic murine tumor model for H&N squamous cell carcinoma and could be visualized after 2 fractions of 10 Gy, whereas in a B16F10 melanoma model upregulation was already observed after 2 × 4 Gy or 2 × 10 Gy fractionated radiotherapy (54). Together, these results demonstrate that regular cancer treatment regimens affect PD-L1 expression, which can be sensitively monitored by noninvasive radionuclide imaging. The effect on PD-L1 expression depends on tumor type, dose, and treatment schedule of the radiotherapy.

Imaging has several advantages over IHC analysis of tumor PD-L1 expression. First, it allows measurement of PD-L1 expression of whole tumor lesions, taking into account intratumoral and interlesional heterogeneity. Second, whole body imaging provides additional information about the PD-L1 status not only in the tumor, but also in normal (hematopoietic) tissues, which could help to better understand the working mechanism of ICI. Third, it allows longitudinal monitoring of PD-L1 expression, which is of clinical relevance because PD-L1 expression can change due to disease progression and/or applied treatment (24, 27, 28). Finally, next to target expression, *in vivo* imaging also accounts for target accessibility. Several factors such as blood vessel density, vascular volume, vascular permeability, and interstitial fluid pressure determine whether antibodies can reach the tumor site and penetrate (55, 56). It is essential that these promising strategies are further translated to the clinic. In preclinical models, microSPECT/CT has a similar or improved resolution compared with microPET/CT. Nevertheless, for clinical studies, PD-L1 antibodies should be preferably radiolabeled with a positron emitter like zirconium-89 (^{89}Zr) for PET/CT imaging, as the resolution, sensitivity, and quantification of PET/CT is superior to that of SPECT/CT. However, it should be taken into account that the current studies are performed in subcutaneous tumor models. Typically, tumor growth and angiogenesis are more rapid in subcutaneous tumor models compared with human tumors. These differences could affect the uptake of the radiolabeled antibodies in the tumor, resulting in different tumor-background ratios in the clinical setting.

Taken together, our results demonstrated that PD-L1 microSPECT/CT could successfully detect tumor PD-L1 expression in tumor-bearing immunocompetent mice, despite high tracer uptake in healthy PD-L1–expressing tissues such as spleen, lymph nodes, duodenum, and brown fat. We also showed that PD-L1 microSPECT/CT was a sensitive imaging method to monitor changes in PD-L1 expression induced by treatment such as ionizing radiation. In clinical practice, this technique holds strong potential to noninvasively select patients who are most likely to respond to ICI therapy and to rationally plan timing of ICI therapy during conventional anticancer treatment based on PD-L1 expression in the tumor lesions.

Disclosure of Potential Conflicts of Interest

D. Olive has ownership interest in Imcheck Therapeutics. No potential conflicts of interest were disclosed by the other authors.

Authors' Contributions

Conception and design: S. Heskamp, O.C. Boerman, H. Dolstra, E.H.J.G. Aarntzen, W.A. Hobo
Development of methodology: S. Heskamp, J.D.M. Molkenboer-Kuenen, J. Cany, D. Olive, O.C. Boerman, W.A. Hobo
Acquisition of data (provided animals, acquired and managed patients, provided facilities, etc.): S. Heskamp, P.J. Wierstra, J.D.M. Molkenboer-Kuenen, G.W. Sandker, S. Thordardottir, J. Bussink, W.A. Hobo
Analysis and interpretation of data (e.g., statistical analysis, biostatistics, computational analysis): S. Heskamp, P.J. Wierstra, J.D.M. Molkenboer-Kuenen, G.W. Sandker, D. Olive, J. Bussink, O.C. Boerman, E.H.J.G. Aarntzen, W.A. Hobo
Writing, review, and/or revision of the manuscript: S. Heskamp, P.J. Wierstra, G.W. Sandker, S. Thordardottir, J. Cany, D. Olive, J. Bussink, O.C. Boerman, H. Dolstra, E.H.J.G. Aarntzen, W.A. Hobo
Administrative, technical, or material support (i.e., reporting or organizing data, constructing databases): S. Heskamp, J.D.M. Molkenboer-Kuenen, S. Thordardottir
Study supervision: S. Heskamp, O.C. Boerman, W.A. Hobo
Other (mAb generation and characterization): D. Olive

Acknowledgments

This study was supported by the Netherlands Organisation for Scientific Research (project number 91617039) and the Dutch Cancer Society (project number 10099). We thank Jasper Lok, Bianca Lemmers-van de Weem, Iris Lamers-Elemans, and Kitty Lemmens-Hermans for technical assistance with the animal experiments.

The costs of publication of this article were defrayed in part by the payment of page charges. This article must therefore be hereby marked *advertisement* in accordance with 18 U.S.C. Section 1734 solely to indicate this fact.

Received April 27, 2018; revised July 23, 2018; accepted November 15, 2018; published first November 20, 2018.

References

1. Riella LV, Paterson AM, Sharpe AH, Chandraker A. Role of the PD-1 pathway in the immune response. Am J Transplant 2012;12:2575–87.
2. Hamid O, Carvajal RD. Anti-programmed death-1 and anti-programmed death-ligand 1 antibodies in cancer therapy. Expert Opin Biol Ther 2013;13:847–61.
3. Saresella M, Rainone V, Al-Daghri NM, Clerici M, Trabattoni D. The PD-1/PD-L1 pathway in human pathology. Curr Mol Med 2012;12:259–67.
4. Ostrand-Rosenberg S, Horn LA, Haile ST. The programmed death-1 immune-suppressive pathway: barrier to antitumor immunity. J Immunol 2014;193:3835–41.

5. Zou W, Chen L. Inhibitory B7-family molecules in the tumour microenvironment. Nat Rev Immunol 2008;8:467–77.
6. Topalian SL, Hodi FS, Brahmer JR, Gettinger SN, Smith DC, McDermott DF, et al. Safety, activity, and immune correlates of anti-PD-1 antibody in cancer. N Engl J Med 2012;366:2443–54.
7. Brahmer JR, Tykodi SS, Chow LQ, Hwu WJ, Topalian SL, Hwu P, et al. Safety and activity of anti-PD-L1 antibody in patients with advanced cancer. N Engl J Med 2012;366:2455–65.
8. Ansell SM, Lesokhin AM, Borrello I, Halwani A, Scott EC, Gutierrez M, et al. PD-1 blockade with nivolumab in relapsed or refractory Hodgkin's lymphoma. N Engl J Med 2015;372:311–9.
9. Brahmer J, Reckamp KL, Baas P, Crino L, Eberhardt WE, Poddubskaya E, et al. Nivolumab versus docetaxel in advanced squamous-cell non-small-cell lung cancer. N Engl J Med 2015;373:123–35.
10. Fury M, Ou SI, Balmanoukian AS, Hansen A, Massarelli E, Blake-Haskins A, et al. 988PD - Clinical activity and safety of MEDI4736, an anti-PD-L1 antibody, in patients with head and neck cancer. Ann Oncol 2014;25 (Supplemental 4).
11. Gibson J. Anti-PD-L1 for metastatic triple-negative breast cancer. Lancet Oncol 2015;16:e264.
12. Motzer RJ, Rini BI, McDermott DF, Redman BG, Kuzel TM, Harrison MR, et al. Nivolumab for metastatic renal cell carcinoma: results of a randomized phase II trial. J Clin Oncol 2015;33:1430–7.
13. McDermott DF, Sosman JA, Sznol M, Massard C, Gordon MS, Hamid O, et al. Atezolizumab, an anti-programmed death-ligand 1 antibody, in metastatic renal cell carcinoma: long-term safety, clinical activity, and immune correlates from a phase IA study. J Clin Oncol 2016;34:833–42.
14. Fehrenbacher L, Spira A, Ballinger M, Kowanetz M, Vansteenkiste J, Mazieres J, et al. Atezolizumab versus docetaxel for patients with previously treated non-small-cell lung cancer (POPLAR): a multicentre, open-label, phase 2 randomised controlled trial. Lancet 2016;387:1837–46.
15. Herbst RS, Baas P, Kim DW, Felip E, Perez-Gracia JL, Han JY, et al. Pembrolizumab versus docetaxel for previously treated, PD-L1-positive, advanced non-small-cell lung cancer (KEYNOTE-010): a randomised controlled trial. Lancet 2015. DOI: 10.1016/S0140-6736(15)01281-7.
16. Naidoo J, Page DB, Li BT, Connell LC, Schindler K, Lacouture ME, et al. Toxicities of the anti-PD-1 and anti-PD-L1 immune checkpoint antibodies. Ann Oncol 2015;26:2375–91.
17. Freeman-Keller M, Kim Y, Cronin H, Richards A, Gibney G, Weber J. Nivolumab in resected and unresectable metastatic melanoma: characteristics of immune-related adverse events and association with outcomes. Clin Cancer Res 2016;22:886–94.
18. Kazandjian D, Khozin S, Blumenthal G, Zhang L, Tang S, Libeg M, et al. Benefit-risk summary of nivolumab for patients with metastatic squamous cell lung cancer after platinum-based chemotherapy: a report from the US Food and Drug Administration. JAMA Oncol 2015:1–5.
19. Taube JM, Klein A, Brahmer JR, Xu H, Pan X, Kim JH, et al. Association of PD-1, PD-1 ligands, and other features of the tumor immune microenvironment with response to Anti-PD-1 Therapy. Clin Cancer Res 2014; 20:5064–74.
20. Grosso J, Horak CE, Inzunza D, Cardona DM, Simon JS, Gupta AK, et al. Association of tumor PD-L1 expression and immune biomarkers with clinical activity in patients (pts) with advanced solid tumors treated with nivolumab (anti-PD-1; BMS-936558; ONO-4538). J Clin Oncol 2013; 31(15).
21. Herbst RS, Gordon MS, Fine GD, Sosman JA, Soria JC, Hamid O, et al. A study of MPDL3280A, an engineered PD-L1 antibody in patients with locally advanced or metastatic tumors. J Clin Oncol 2013;31(15).
22. Peters S, Gettinger S, Johnson ML, Janne PA, Garassino MC, Christoph D, et al. Phase II trial of atezolizumab as first-line or subsequent therapy for patients with programmed death-ligand 1-selected advanced non-small-cell lung cancer (BIRCH). J Clin Oncol 2017;35:2781–9.
23. Kerr KM, Tsao MS, Nicholson AG, Yatabe Y, Wistuba II, Hirsch FR, et al. Programmed death-ligand 1 immunohistochemistry in lung cancer: in what state is this art? J Thorac Oncol 2015;10:985–9.
24. Dong H, Strome SE, Salomao DR, Tamura H, Hirano F, Flies DB, et al. Tumor-associated B7-H1 promotes T-cell apoptosis: a potential mechanism of immune evasion. Nat Med 2002;8:793–800.
25. Joseph RW, Parasramka M, Eckel-Passow JE, Serie D, Wu K, Jiang L, et al. Inverse association between programmed death ligand 1 and genes in the VEGF pathway in primary clear cell renal cell carcinoma. Cancer Immunol Res 2013;1:378–85.
26. Kondo A, Yamashita T, Tamura H, Zhao W, Tsuji T, Shimizu M, et al. Interferon-gamma and tumor necrosis factor-alpha induce an immunoinhibitory molecule, B7-H1, via nuclear factor-kappaB activation in blasts in myelodysplastic syndromes. Blood 2010;116:1124–31.
27. Ghebeh H, Lehe C, Barhoush E, Al-Romaih K, Tulbah A, Al-Alwan M, et al. Doxorubicin downregulates cell surface B7-H1 expression and upregulates its nuclear expression in breast cancer cells: role of B7-H1 as an anti-apoptotic molecule. Breast Cancer Res 2010;12:R48.
28. Zhang P, Su DM, Liang M, Fu J. Chemopreventive agents induce programmed death-1-ligand 1 (PD-L1) surface expression in breast cancer cells and promote PD-L1-mediated T cell apoptosis. Mol Immunol 2008; 45:1470–6.
29. Deng L, Liang H, Burnette B, Beckett M, Darga T, Weichselbaum RR, et al. Irradiation and anti-PD-L1 treatment synergistically promote antitumor immunity in mice. J Clin Invest 2014;124:687–95.
30. Scala S. Molecular pathways: targeting the CXCR4-CXCL12 axis-untapped potential in the tumor microenvironment. Clin Cancer Res 2015;21: 4278–85.
31. Dovedi SJ, Adlard AL, Lipowska-Bhalla G, McKenna C, Jones S, Cheadle EJ, et al. Acquired resistance to fractionated radiotherapy can be overcome by concurrent PD-L1 blockade. Cancer Res 2014;74:5458–68.
32. Du Four S, Maenhout SK, De Pierre K, Renmans D, Niclou SP, Thielemans K, et al. Axitinib increases the infiltration of immune cells and reduces the suppressive capacity of monocytic MDSCs in an intracranial mouse melanoma model. Oncoimmunology 2015;4:e998107.
33. Lim SH, Hong M, Ahn S, Choi YL, Kim KM, Oh D, et al. Changes in tumour expression of programmed death-ligand 1 after neoadjuvant concurrent chemoradiotherapy in patients with squamous oesophageal cancer. Eur J Cancer 2016;52:1–9.
34. Callea M, Albiges L, Gupta M, Cheng SC, Genega EM, Fay AP, et al. Differential expression of PD-L1 between primary and metastatic sites in clear-cell renal cell carcinoma. Cancer Immunol Res 2015;3:1158–64.
35. Jilaveanu LB, Shuch B, Zito CR, Parisi F, Barr M, Kluger Y, et al. PD-L1 expression in clear cell renal cell carcinoma: an analysis of nephrectomy and sites of metastases. J Cancer 2014;5:166–72.
36. Madore J, Vilain R, Menzies AM, Kakavand H, Wilmott JS, Hyman J, et al. PD-L1 expression in melanoma shows marked heterogeneity within and between patients: implications for anti-PD-1/PD-L1 clinical trials. Pigment Cell Melanoma Res 2015;28:245–53.
37. Fusi A, Festino L, Botti G, Masucci G, Melero I, Lorigan P, et al. PD-L1 expression as a potential predictive biomarker. Lancet Oncol 2015;16: 1285–7.
38. Ilie M, Long-Mira E, Bence C, Butori C, Lassalle S, Bouhlel L, et al. Comparative study of the PD-L1 status between surgically resected specimens and matched biopsies of NSCLC patients reveal major discordances. A potential issue for anti-PD-L1 therapeutic strategies. Ann Oncol 2016;27:147–53.
39. Muller P, Rothschild SI, Arnold W, Hirschmann P, Horvath L, Bubendorf L, et al. Metastatic spread in patients with non-small cell lung cancer is associated with a reduced density of tumor-infiltrating T cells. Cancer Immunol Immunother 2015;65:1–11.
40. Heskamp S, Hobo W, Molkenboer-Kuenen JD, Olive D, Oyen WJ, Dolstra H, et al. Noninvasive imaging of tumor PD-L1 expression using radiolabeled anti-PD-L1 antibodies. Cancer Res 2015;75:2928–36.
41. Ghiotto M, Gauthier L, Serriari N, Pastor S, Truneh A, Nunes JA, et al. PD-L1 and PD-L2 differ in their molecular mechanisms of interaction with PD-1. Int Immunol 2010;22:651–60.
42. van der Have F, Vastenhouw B, Ramakers RM, Branderhorst W, Krah JO, Ji C, et al. U-SPECT-II: an ultra-high-resolution device for molecular small-animal imaging. J Nucl Med 2009;50:599–605.
43. van Dijk LK, Boerman OC, Franssen GM, Kaanders JH, Bussink J. 111In-cetuximab-F(ab')2 SPECT and 18F-FDG PET for prediction and response monitoring of combined-modality treatment of human head and neck carcinomas in a mouse model. J Nucl Med 2015;56:287–92.
44. Press OW, Shan D, Howell-Clark J, Eary J, Appelbaum FR, Matthews D, et al. Comparative metabolism and retention of iodine-125, yttrium-90, and indium-111 radioimmunoconjugates by cancer cells. Cancer Res 1996;56:2123–9.

45. Mayer AT, Natarajan A, Gordon SR, Maute RL, McCracken MN, Ring AM, et al. Practical Immuno-PET radiotracer design considerations for human immune checkpoint imaging. J Nucl Med 2017;58: 538–46.
46. Chatterjee S, Lesniak WG, Gabrielson M, Lisok A, Wharram B, Sysa-Shah P, et al. A humanized antibody for imaging immune checkpoint ligand PD-L1 expression in tumors. Oncotarget 2016;7: 10215–27.
47. Lesniak WG, Chatterjee S, Gabrielson M, Lisok A, Wharram B, Pomper MG, et al. PD-L1 detection in tumors using [(64)Cu]atezolizumab with PET. Bioconjug Chem 2016;27:2103–10.
48. Chatterjee S, Lesniak WG, Miller MS, Lisok A, Sikorska E, Wharram B, et al. Rapid PD-L1 detection in tumors with PET using a highly specific peptide. Biochem Biophys Res Commun 2017;483: 258–63.
49. Gonzalez Trotter DE, Meng X, McQuade P, Rubins D, Klimas M, Zhang Z, et al. In vivo imaging of the programmed death ligand 1 by 18F positron emission tomography. J Nucl Med 2017;58:1852–7.
50. Hettich M, Braun F, Bartholoma MD, Schirmbeck R, Niedermann G. High-resolution PET imaging with therapeutic antibody-based PD-1/PD-L1 checkpoint tracers. Theranostics 2016;6:1629–40.
51. Josefsson A, Nedrow JR, Park S, Banerjee SR, Rittenbach A, Jammes F, et al. Imaging, biodistribution, and dosimetry of radionuclide-Labeled PD-L1 antibody in an immunocompetent mouse model of breast cancer. Cancer Res 2016;76:472–9.
52. Nedrow JR, Josefsson A, Park S, Ranka S, Roy S, Sgouros G. Imaging of programmed death ligand-1 (PD-L1): impact of protein concentration on distribution of anti-PD-L1 SPECT agent in an immunocompetent melanoma murine model. J Nucl Med 2017;58:1560–66.
53. Broos K, Keyaerts M, Lecocq Q, Renmans D, Nguyen T, Escors D, et al. Non-invasive assessment of murine PD-L1 levels in syngeneic tumor models by nuclear imaging with nanobody tracers. Oncotarget 2017;8: 41932–46.
54. Kikuchi M, Clump DA, Srivastava RM, Sun L, Zeng D, Diaz-Perez JA, et al. Preclinical immunoPET/CT imaging using Zr-89-labeled anti-PD-L1 monoclonal antibody for assessing radiation-induced PD-L1 upregulation in head and neck cancer and melanoma. Oncoimmunology 2017;6: e1329071.
55. Heldin CH, Rubin K, Pietras K, Ostman A. High interstitial fluid pressure - an obstacle in cancer therapy. Nat Rev Cancer 2004;4:806–13.
56. Jain RK. Transport of molecules, particles, and cells in solid tumors. Annu Rev Biomed Eng 1999;1:241–63.